ChemComm

COMMUNICATION

View Article Online
View Journal | View Issue

Cite this: *Chem. Commun.*, 2024, **60**, 10528

Received 2nd July 2024,
Accepted 20th August 2024

DOI: 10.1039/d4cc03296a

rsc.li/chemcomm

One-dimensional hybrid copper halides with high-efficiency photoluminescence as scintillator†

Zhongliang Gong,‡[a] Jie Zhang,‡[ab] Ying-Yue Liu,[a] Lu-Xin Zhang,[a] Qing Zhang,[a] Lingyun Xiao,[a] Bingqiang Cao,*[b] Bing Hu *[c] and Xiao-Wu Lei *[a]

A new one-dimensional hybrid [APCHA]Cu_2I_4 was designed and applied as an X-ray scintillator. It exhibits broad-band green emission with a high PLQY of 74.80% and excellent stability. It demonstrates radioluminescence property with a light yield of 28 336 photons MeV^{-1}, detection limit of 41 nGy_{air} s^{-1}, and high spatial limit of 13.95 lp mm^{-1} in X-ray imaging.

Semiconducting metal halides have sparked significant research interest due to their excellent optical properties and promising practical applications in photovoltaics, light-emitting diodes, photoelectric detectors, and scintillators.[1–5] Especially, scintillators can convert high-energy radiation into visible or near-infrared light, broadly used in medical diagnostics, security detection, and space exploration.[6–10] Three-dimensional (3D) all-inorganic perovskite nanocrystals of $CsPbX_3$ (X = Cl, Br, I) showed unique advantages as scintillators owing to their simple synthesis method, tunable photoluminescence (PL) wavelength, and negligible afterglow.[11–14] However, the inherent toxicity of Pb^{2+} and the instability of perovskite nanocrystals hinder their application in more sophisticated and extensive optical devices. Therefore, it is urgent to explore lead-free, low-cost, and diverse luminous metal halides at the molecular level.

Recently, a series of lead-free low-dimensional metal halides (LDMHs) with good PL performance have emerged. Owing to their various organic cations and abundant metal centers (In^{3+}, Sb^{3+}, Cd^{2+}, Cu^{+}, Zn^{2+}), LDMHs offered more varied spatial arrangement structures and tunable PL properties, making them promising candidates in LEDs, displays, and X-ray detectors.[15–19] Furthermore, the inherent quantum confinement endows LDMHs with highly localized excitons and high luminescent efficiency. For example, featuring ns^2 electron configuration, the Sb^{3+}-based organic–inorganic hybrid of $C_{50}H_{44}P_2SbCl_5$ crystal demonstrated strong yellow light emission with a near-unity PL quantum yield (PLQY) of 98.42% when excited by 370-nm light. This material also showed great environmental and irradiation stability, with a good linear response to X-ray dose rates and a light yield of 44 460 photons MeV^{-1}.[20] Sun *et al.* developed a $[DBA]_4Cu_4I_4$ wafer with a high PLQY of 94.9%, which demonstrated a light yield higher than 1×10^4 photons MeV^{-1} and a high spatial resolution of 5.0 lp mm^{-1}, showing potential in practical X-ray imaging applications.[21] Mohammed *et al.* reported a 0D $Cu_4I_4L_4$ crystal with a broad emission band and a high PLQY above 85%, exhibiting a high light yield of 30 000 photons MeV^{-1} and a low detection limit of 150 nGy s^{-1}.[22] A manganese-based hybrid $(C_{38}H_{34}P_2)MnBr_4$ exhibits narrow green light emission with a high light yield of 80 000 photons MeV^{-1}, a low detection limit of 72.8 nGy s^{-1} and a strong afterglow of 10 ms.[23] Nevertheless, although organic–inorganic metal halides are very promising luminescent materials, the low light yields of Sb^{3+}-based hybrids and the long afterglow of Mn^{2+}-based hybrids limited their applications in scintillation materials field. Recently, low-dimensional cuprous halides have demonstrated unique superiorities as scintillators due to their nanosecond afterglow, shedding light on the way forward for the research of metal halide scintillators.[24] Short afterglow, high light yields, and various spatial arrangement structures offer copper-based hybrids with advantages as scintillators.

Inspired by the previous study, we decided to focus on X-ray scintillation materials and strive to explore Cu-based halides in this field. In this work, 1D copper halide of [APCHA]Cu_2I_4 (APCHA = *N*-(3-aminopropyl)cyclohexylamine) was assembled using a simple solvent method. Under the excitation of ultraviolet light, [APCHA]Cu_2I_4 displays strong green light emission with a high PLQY of 74.80%. Furthermore, as a scintillation

[a] *Research Institute of Optoelectronic Functional Materials, School of Chemistry, Chemical Engineering and Materials, Jining University, Qufu, Shandong, 273155, P. R. China. E-mail: xwlei_jnu@163.com*
[b] *School of Material Science and Engineering, University of Jinan, Jinan, Shandong, 250022, P. R. China. E-mail: mse_caobq@ujn.edu.cn*
[c] *State Key Laboratory of Structural Chemistry, Fujian Institute of Research on the Structure of Matter, Chinese Academy of Sciences, Fuzhou, Fujian 350002, P. R. China. E-mail: hubing@fjirsm.ac.cn*

† Electronic supplementary information (ESI) available: Experimental, theoretical, analytical and crystallographic details. CCDC 2361461. For ESI and crystallographic data in CIF or other electronic format see DOI: https://doi.org/10.1039/d4cc03296a

‡ These authors contributed equally to this work.

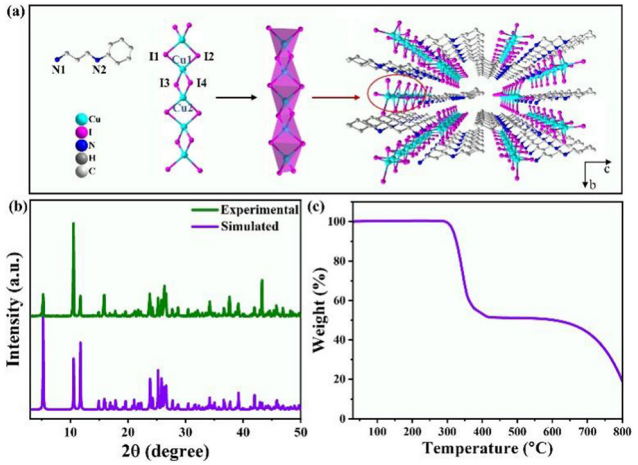

Fig. 1 (a) The detailed and arrangement structure of [APCHA]Cu_2I_4. (b) The simulated and experimental PXRD patterns of [APCHA]Cu_2I_4. (c) TGA curve of [APCHA]Cu_2I_4.

material, [APCHA]Cu_2I_4 revealed radioluminescence with a light yield of 28 336 photons MeV^{-1} and a detection limit of 41 nGy_{air} s^{-1}. In addition, the halide exhibits good optical stability when exposed to air and X-ray doses. This work paves the way for the designing of copper-based metal halides in X-ray imaging and detectors.

A high-quality [APCHA]Cu_2I_4 crystal was synthesized at room temperature using a saturated crystallization method. The single crystal was identified as belonging to the $P2_1$ space group within a monoclinic system, composed of $[APCHA]^{2+}$ organic cations and $[Cu_2I_4]^{2-}$ chains (Fig. 1a). The configuration of the distorted $[Cu_2I_4]^{2-}$ chain is formed by two approximately mirror-symmetric tetrahedra with Cu–I bond lengths in a normal range of 0.259–0.281 Å.[25] The 1D $[Cu_2I_4]^{2-}$ chains are separated and surrounded by organic cations, forming a hybrid structure with abundant hydrogen bonds between them. The PXRD pattern of [APCHA]Cu_2I_4 crystal matches well with the simulated result from single-crystal data, confirming high purity without impurity (Fig. 1b). Thermogravimetric analysis (TGA) shown in Fig. 1c reveals a sharp weight loss when the temperature was above 280 °C, suggesting good thermostability of [APCHA]Cu_2I_4. When the temperature reached 420 °C, the crystal melted and decomposed with the organic species evaporating completely, leaving the final substance of cuprous iodide (Fig. S1, ESI†).

UV-vis absorption spectrum shown in Fig. 2a features a broad band with several sub-bands in the range 200–750 nm and a sharp slope, corresponding to a bandgap of 2.68 eV from the Tauc's Plot. Owing to the partial absorption in the visible region, this crystal appears light pink under daylight. It exhibits green light emission under excitation of 254 nm UV light (Fig. 2b). To understand the luminescence mechanism, we recorded the PL excitation (PLE) and PL spectra of the [APCHA]-Cu_2I_4 crystal (Fig. S2 and S3, ESI†). Monitoring the wavelength of the maximum emission peak at 498 nm, the excitation spectrum consisted of an intense band with a maximum peak of 296 nm and a shoulder peak around 270 nm. Upon UV

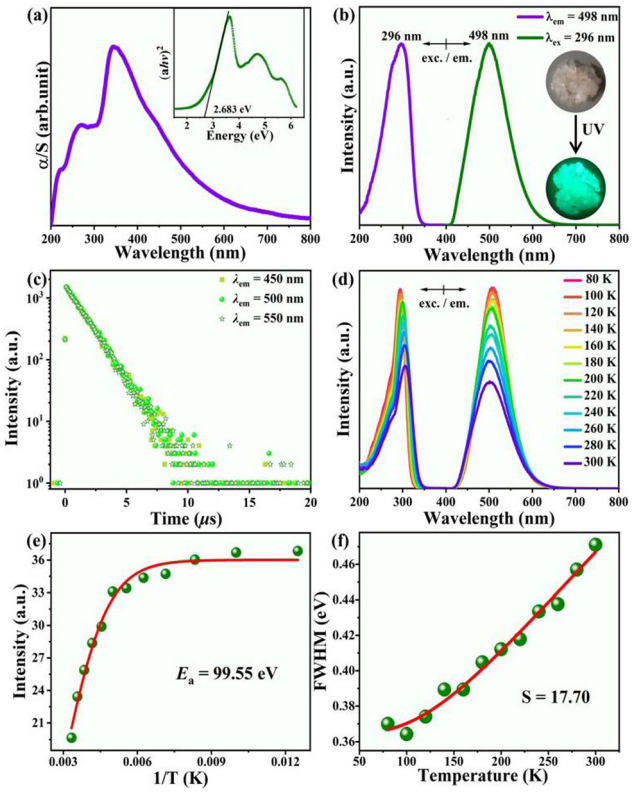

Fig. 2 (a) Optical absorption spectrum of [APCHA]Cu_2I_4 with the corresponding Tauc Plot. (b) PLE and PL spectrum of [APCHA]Cu_2I_4 with inset photos under daylight and UV light. (c) The PL decay curves (λ_{ex} = 296 nm) of the halide. (d) Temperature-dependent PLE spectra (λ_{em} = 498 nm) and PL spectra (λ_{ex} = 296 nm) of the halide. (e) The experimental and fitted PL intensity as a function of reciprocal temperature. (f) Temperature-dependent FWHM and fitting data.

excitation at 296 nm, the halide exhibited a single broad emission band with a full width at half maximum (FWHM) of ≈492.8 meV. The Commission Internationale del'Eclairage (CIE) chromaticity coordinates were (0.18, 0.36) and the absolute PLQY of 74.80% (Fig. S4 and S5, ESI†). Furthermore, by monitoring different emission wavelengths, the time-resolved PL decay curves showed an identical long-lived monoexponential decay lifetime of 1.332 μs. This indicates that there is only one radiative carrier recombination pathway in this compound (Fig. 2c).

To gain deep insights into the excited-stated dynamics of [APCHA]Cu_2I_4 crystal, we measured the temperature-dependent PL spectra in the range of 80–300 K. As shown in Fig. 2d, both the excitation and emission spectra reveal a gradual decrease in intensity and a broadening of the bandwidth with increasing temperature. Moreover, the PL lifetimes decrease from 2.124 to 1.431 μs, due to enhanced electron–phonon coupling accelerating nonradiative relaxation (Fig. S6 and Table S4, ESI†). Temperature-dependent PL intensity and FWHM provide information about the compound's activation energy (E_a) and electron–phonon coupling strength. A higher E_a value of 99.55 meV is obtained by fitting the integrated PL intensity as a function of inverse temperature based on the Arrhenius function.This value is higher than the room

temperature thermal energy (~25 meV), indicating excellent stability of the excitons (Fig. 2e). The Huang–Rhys factor (S), representing electron–phonon coupling parameter, is fitted by the equation with the FWHM as a function of temperature. Compared to the inorganic halides $Cs_3Cu_2I_5$ (40.33)[26] and $CsCu_2I_3$ (38.4),[27] [APCA]Cu_2I_4 has a smaller S value of 17.70, suggesting weaker electron–phonon coupling, which is consistent with the compact tetrahedral coordination (Fig. 2f).

To gain deeper insight into the photophysical properties of [APCHA]Cu_2I_4, we performed density functional theory (DFT) calculations on the band structure and density of states (DOS).

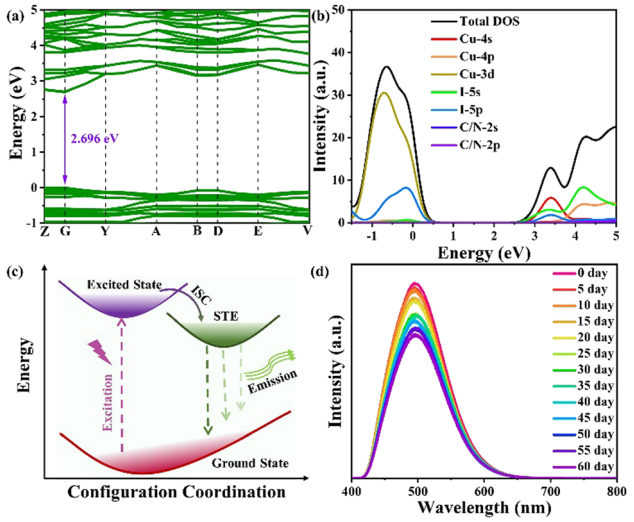

Fig. 3 Electronic band structures (a) and densities of state (b) for the [APCHA]Cu_2I_4 computed by DFT. (c) Schematic PL mechanism of [APCHA]Cu_2I_4. (d) Time-dependent PL spectra of [APCHA]Cu_2I_4.

The results reveal that [APCHA]Cu_2I_4 has a direct bandgap of 2.696 eV with both valence band maximum (VBM) and conduction band minimum (CBM) being at G point, which is in good agreement with the experimental results from the absorption spectrum (Fig. 3a). The VBM is mostly contributed by Cu-3d state while the CBM mainly comprises Cu-4s and I-5s states (Fig. 3b). Therefore, the excited electron is generally located on the $[Cu_2I_4]^{2-}$ chain. Based on the above analysis, the photophysical process of [APCHA]Cu_2I_4 is depicted in the diagram as shown in Fig. 3c. Upon excitation with UV light, the electrons transition from the ground state to an excited state. The exciton–phonon interaction then leads to the formation of STEs from free carriers, followed by radiative decay from STEs as broad-band emission. In addition, [APCHA]Cu_2I_4 exhibits superior optical stability, as evidenced by an unchanged XRD pattern and sufficient PL emission intensity after being stored in humid air for 2 months (Fig. 3d and Fig. S7, ESI†). The sample of [APCHA]Cu_2I_4 also exhibits structural and spectral stability toward various organic solutions, such as acetone, acetonitrile, and dichloromethane, for one day. (Fig. S8 and S9, ESI†).

The [APCHA]Cu_2I_4 crystal also exhibits bright green light under X-ray irradiation, which benefits from high PLQY and large Stokes shift (Fig. 4a). The similar radioluminescence (RL) and PL emission bands indicate the same recombination pathway under both X-ray and UV light. The absorption coefficient of [APCHA]Cu_2I_4, one of the critical performance indicators, as a function of X-ray photon energy is smaller than that of LuAG: Ce, due to its lower-atomic-number elements (Fig. 4b). The scintillation light yield of [APHCA]Cu_2I_4 is calculated to be 28 336 photons MeV^{-1} by using a commercially available LuAG: Ce as standard reference (Fig. 4c). The detection limit is a key parameter for evaluating the performance of X-ray scintillators. When irradiated with an X-ray

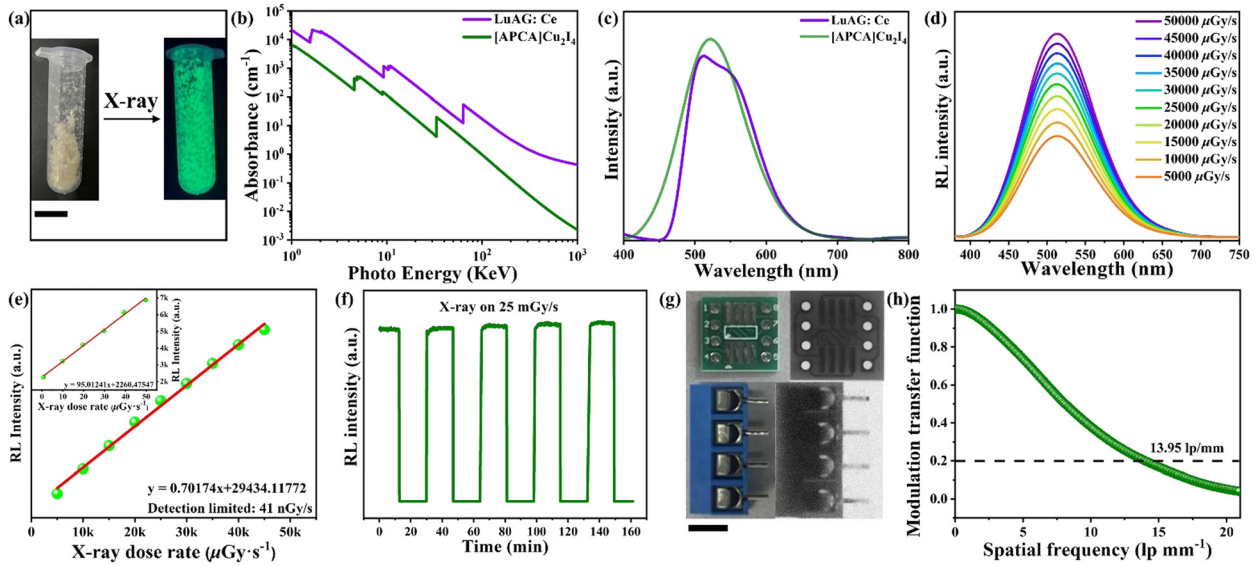

Fig. 4 (a) The photos of [APCHA]Cu_2I_4 under daylight and X-ray dose (scale bar = 5 mm). Comparison of absorption coefficients (b) and RL emission (c) of LuAG: Ce and [APCHA]Cu_2I_4. (d) RL emission spectra of [APCHA]Cu_2I_4 at different X-ray dose rates. (e) The X-ray dose rate-dependent RL intensity of [APCHA]Cu_2I_4. (f) Temporal response of [APCHA]Cu_2I_4 under 25 mGy s^{-1} dose rate. (g) X-ray images and photos of the chips (scale bar = 5 mm). (h) MTF curve of thin film.

dose rate in the range of 5000–50 000 $\mu Gy_{air}\ s^{-1}$, the RL emission spectra revealed that [APCHA]Cu_2I_4 shows a linear response to the X-ray dose rate with a low detection limit of 41 $nGy_{air}\ s^{-1}$ (Fig. 4d and e). Fig. 4f shows the temporal response of the [APCHA]Cu_2I_4 under a square-wave modulated X-ray dose of 25 $mGy_{air}\ s^{-1}$, indicating excellent repeatability and stability under X-ray irradiation. In addition, we prepared a film by mixing microscale [APCHA]Cu_2I_4 with polydimethylsiloxane (PDMS) to verify its X-ray imaging performance (Fig. S8, ESI†). The metal wire embedded in the integrated circuit can be clearly distinguished in the scintillator screen under X-ray irradiation owing to the difference in the absorption intensity of different materials (Fig. 4g). To further evaluate the image quality, the modulation transfer function (MTF) is calculated based on the slanted-edge method, which gives a spatial resolution of 13.95 lp mm^{-1} at an MTF value of 0.2 (Fig. 4h).

In summary, we successfully synthesized a new LDMH of [APCHA]Cu_2I_4 using a room-temperature saturated crystallization method. Excited by UV light at 300 nm, this crystal displays bright green light with a high PLQY of 74.80% originating from the STE recombination process. Furthermore, this compound exhibits intensive scintillation performance with a light yield of 28 336 photons MeV^{-1} and a detection limit of 41 $nGy_{air}\ s^{-1}$ under X-ray irradiation. This work thus provides a new structural platform for the application in optoelectronic devices and promotes the potential application as scintillation materials. We believe this work will encourage the development of molecular-level optoelectronic devices by demonstrating the great application potential of low-dimensional hybrid Cu-based halides.

We express thanks for financial support from the National Nature Science Foundation of China (22171105), Shandong Provincial Natural Science Foundation (ZR2022YQ14 and ZR2021MB001), and Special Foundation of Taishan Scholar Project.

Data availability

The data that support the findings of this study are available in the ESI† of this article.

Conflicts of interest

There are no conflicts to declare.

Notes and references

1 X. C. Wang, T. X. Bai, J. L. Sun, J. Y. Liu, Y. Su and J. S. Chen, *Chem. Eng. J.*, 2024, **486**, 150257.
2 D. H. Liang, H. B. Xiao, W. S. Cai, S. R. Lu, S. Y. Zhao, Z. G. Zang and L. Xie, *Adv. Opt. Mater.*, 2023, **11**, 2202997.
3 S. S. Li, P. F. Cheng, H. X. Liu, J. T. Li, S. J. Wang, C. L. Xiao, J. Y. Liu, J. S. Chen and K. F. Wu, *Angew. Chem., Int. Ed.*, 2024, **63**, e202319969.
4 D. H. Chang, Y. P. Chen, L. R. Wang, J. X. Wang, Y. J. Feng, Y. F. Yuan, H. Gao, M. Wu, R. J. Fu, G. Yang, K. Wang and H. Z. Guo, *Adv. Opt. Mater.*, 2024, **12**, 2302829.
5 J. Zhang, X. Wang, W. Q. Wang, X. Y. Deng, C. Y. Yue, X. W. Lei and Z. L. Gong, *Inorg. Chem.*, 2024, **63**, 2647–2654.
6 L. Zi, J. Song, N. Wang, T. Y. Wang, W. Li, H. C. Zhu, W. Xu and H. W. Song, *Laser Photonics Rev.*, 2023, **17**, 2200852.
7 H. M. Chen, M. Lin, C. B. Zhao, D. W. Zhang, Y. Zhang, F. H. Chen, Y. Chen, X. Fang, Q. Liao, H. Meng and M. J. Lin, *Adv. Opt. Mater.*, 2023, **11**, 2300365.
8 H. P. Xu, W. Q. Liang, Z. Z. Zhang, C. Cao, W. S. Yang, H. M. Zeng, Z. E. Lin, D. W. Zhao and G. H. Zou, *Adv. Mater.*, 2023, **35**, 2300136.
9 Z. Z. Zhang, Z. L. He, J. B. Luo, J. H. Wei, X. X. Guo, J. H. Chen and D. B. Kuang, *Adv. Opt. Mater.*, 2024, **12**, 2302434.
10 D. Y. Li, Y. B. Shang, Q. Liu, H. W. Zhang, X. Y. Zhang, C. Y. Yue and X. W. Lei, *Mater. Horiz.*, 2023, **10**, 5004–5015.
11 S. H. Shi, H. H. Yao, D. X. Chen, Z. Z. Li, Z. Xu and Q. Wang, *Adv. Opt. Mater.*, 2023, **11**, 2300795.
12 X. C. Wu, Z. Guo, S. Zhu, B. B. Zhang, S. M. Guo, X. H. Dong, L. Q. Mei, R. X. Liu, C. J. Su and Z. J. Gu, *Adv. Sci.*, 2022, **9**, 2200831.
13 W. B. Ma, T. M. Jiang, Z. Yang, H. Zhang, Y. R. Su, Z. Chen, X. Y. Chen, Y. G. Ma, W. J. Zhu, X. Yu, H. M. Zhu, J. B. Qiu, X. Liu, X. H. Xu and Y. Yang, *Adv. Sci.*, 2021, **8**, 2003728.
14 H. Y. Chen, Q. Wang, G. Q. Peng, S. Wang, Y. T. Lei, H. X. Wang, Z. Yang, J. Sun, N. Li, L. Zhao, W. Lan and Z. W. Jin, *Adv. Opt. Mater.*, 2022, **10**, 2102790.
15 M. S. Molokeev, B. B. Su, A. S. Aleksandrovsky, N. N. Golovnev, M. E. Plyaskin and Z. G. Xia, *Chem. Mater.*, 2022, **34**, 537–546.
16 Z. Tang, X. Meng, H. Y. Zhao, S. J. Ji, Q. J. Wang, T. X. Bai, R. L. Zhang, J. K. Jiang, C. Katan, J. Even and F. Liu, *Adv. Opt. Mater.*, 2024, **12**, 2301282.
17 X. Meng, S. J. Ji, Q. J. Wang, X. C. Wang, T. X. Bai, R. L. Zhang, B. Yang, Y. M. Li, Z. P. Shao, J. K. Jiang, K. L. Han and F. Liu, *Adv. Sci.*, 2022, **9**, 2203596.
18 G. D. Zhang, P. P. Dang, H. Xiao, H. Z. Lian, S. Liang, L. Yang, Z. Y. Cheng, G. G. Li and J. Lin, *Adv. Opt. Mater.*, 2021, **9**, 2101637.
19 S. H. He, S. Q. Hao, L. B. Fan, K. J. Liu, C. X. Cai, C. Wolverton, J. Zhao and Q. L. Liu, *Adv. Opt. Mater.*, 2023, **11**, 2300218.
20 H. X. Meng, B. Chen, W. J. Zhu, Z. J. Zhou, T. X. Jiang, X. W. Xu, S. J. Liu and Q. Zhao, *Laser Photonics Rev.*, 2023, **17**, 2201007.
21 Q. S. Hu, C. K. Zhang, X. Wu, G. J. Liang, L. Wang, X. W. Niu, Z. Wang, W. D. Si, Y. B. Han, R. Q. Huang, J. W. Xiao and D. Sun, *Angew. Chem. Int. Ed.*, 2023, **135**, e202217784.
22 Y. Zhou, T. Y. He, P. Yuan, J. Yin, S. L. Chen, L. Gutiérrez-Arzaluz, L. J. Wang, O. M. Bakr and O. F. Mohammed, *ACS Mater. Lett.*, 2023, **5**, 2002–2008.
23 L. J. Xu, X. S. Lin, Q. Q. He, M. Worku and B. W. Ma, *Nat. Commun.*, 2020, **11**, 4329.
24 T. T. Xu, Y. Y. Li, M. Nikl, R. Kucerkova, Z. Y. Zhou, J. Chen, Y. Y. Sun, G. D. Niu, J. Tang, Q. Wang, G. H. Ren and Y. T. Wu, *ACS Appl. Mater. Interfaces*, 2022, **14**, 14157–14164.
25 H. Z. Chen, D. L. Wang, R. X. Hou, D. F. Sun, L. Q. Meng, K. Wu, J. Y. Wang and C. Y. Shen, *ACS Appl. Mater. Interfaces*, 2024, **16**, 10325–10334.
26 L. Y. Lian, M. Y. Zheng, W. Z. Zhang, L. X. Yin, X. Y. Du, P. Zhang, X. W. Zhang, J. B. Gao, D. L. Zhang, L. Gao, G. D. Niu, H. S. Song, R. Chen, X. Z. Lan, J. Tang and J. B. Zhang, *Adv. Sci.*, 2020, **7**, 2000195.
27 Z. Z. Ma, Z. F. Shi, C. C. Qin, M. H. Cui, D. W. Yang, X. J. Wang, L. T. Wang, X. Z. Ji, X. Chen, J. L. Sun, D. Wu, Y. Zhang, X. J. Li, L. J. Zhang and C. X. Shan, *ACS Nano*, 2020, **14**, 4475–4486.